Impact of Orbital Characteristics and Viewing Geometry on the Retrieval of Cloud Properties From Multiangle Polarimetric Measurements

Yutong Wang, Huazhe Shang, Husi Letu, *Senior Member, IEEE*, Lesi Wei, Feinan Chen, Jin Hong, Zhongting Wang, and Liangfu Chen

***Abstract*— Clouds play an important role in the radiative energy balance of the Earth–atmosphere system. Compared with traditional optical satellite sensors, polarimetric sensors combine multiangle, multipolarization, and multispectral information, displaying the advantages of high spatial and temporal resolutions and global coverage. Such remote sensing measurements improve the accuracy of cloud properties retrieval. Due to the observation characteristics of passive satellites, even a tiny variation in position will result in a great change in the observation geometry. A large number of studies have shown that the scattering angle is very crucial for the polarization characteristics retrieval of reflected light. In this study, we analyze the dependence of the remote sensing retrieval implementation of different cloud characteristics on the observed scattering angle coverage, considering both ice and water clouds. Three satellite sensors—POLarization and Directionality of the Earth's Reflectance-3/Polarization and Anisotropy of Reflectance for Atmospheric Sciences coupled with Observations from a Lidar (POLDER-3/PARASOL), Directional Polarimetric Camera/GaoFen-5 spacecraft (DPC/GF-5), and DPC/GF-5(02)—were selected to compare their scattering angle coverages and the number of angular measurements at equatorial, middle, and high latitudes. The requirements for angular polarized and nonpolarized observations varied depending on the retrieval of cloud properties. The impact of orbital characteristics and viewing settings was investigated for cloud detection (C-Det), cloud phase classification, and cloud microphysical properties retrieval. Finally, an analytical model to comprehensively evaluate the effective angular measurements according to the orbital characteristics and viewing settings was developed to facilitate the future design of similar sensors for cloud remote sensing.**

***Index Terms*— Cloud retrieval, directional polarimetric camera (DPC), observation geometry, POLarization and Directionality of the Earth's Reflectance-3 (POLDER-3), polarization multiangle payload, scattering angle.**

Manuscript received 11 May 2023; revised 28 September 2023; accepted 27 October 2023. Date of publication 1 November 2023; date of current version 17 November 2023. This work was supported in part by the National Natural Science Foundation of China under Grant 42025504 and Grant 42175152, and in part by the Youth Innovation Promotion Association of Chinese Academy of Sciences under Grant 2021122. *(Corresponding authors: Huazhe Shang; Husi Letu.)*

Yutong Wang is with the State Key Laboratory of Remote Sensing Science, Aerospace Information Research Institute, Chinese Academy of Sciences, Beijing 100101, China, and also with the University of Chinese Academy of Sciences, Beijing 100049, China (e-mail: wangyutong221@mails.ucas.ac.cn).

Huazhe Shang, Husi Letu, Lesi Wei, and Liangfu Chen are with the State Key Laboratory of Remote Sensing Science, Aerospace Information Research Institute, Chinese Academy of Sciences, Beijing 100101, China (e-mail: shanghz@radi.ac.cn; husiletuw@hotmail.com; weils@aircas.ac.cn; chenlf@radi.ac.cn).

Feinan Chen and Jin Hong are with the Anhui Institute of Optics and Fine Mechanics, Hefei Institutes of Physical Science, Chinese Academy of Sciences, Hefei 230031, China (e-mail: feinan123@aiofm.ac.cn; hongjin@aiofm.ac.cn).

Zhongting Wang is with the Satellite Environmental Center, Ministry of Environmental Protection, Beijing 100094, China (e-mail: wzt_07@126.com).

Digital Object Identifier 10.1109/TGRS.2023.3329305

I. Introduction

CLOUDS have a two-sided nature. As an indispensable and significant aspect of the Earth system, clouds have been widely used in the monitoring, analysis, and prediction of climate change, atmospheric circulation, the Earth's hydrologic cycle, and the radiative energy balance of the Earth-atmosphere system [1], [2], [3], [4], [5], [6], [7], [8], [9], [10]. However, they significantly hinder the signal transmission between satellite sensors and ground facilities, generally affecting the quality of remote sensing images [11], [12]. The importance of clouds is self-evident, and their accurate and effective observation has been frequently studied. The polarization multiangle imager is widely regarded as a crucial device for providing multidimensional information for global and regional cloud retrieval. The simultaneous spectral, angular, and polarization information of atmospheric radiation that it provides can maximize the sensitivity of observational data to fine cloud parameters [13]. Compared with traditional optical satellite payloads, the polarization multiangle observation payload couples multiangle, multipolarization, and multispectral information, displaying the advantages of high spatial and temporal resolution, real-time continuity, regional-scale monitoring, and global coverage [14]. Moreover, it addresses gaps in information relating to polarization characteristics and observation angles [15]. The polarization multiangle observation payload improves the accuracy of cloud characterization and has become a vital source of information for the stereo detection of cloud characteristics [16], [17], [18].

There has been substantial global progress in the development of polarized multiangle payloads over the past 30 years. These advancements include: 1) gradual increase in polarization observation bands of payloads; 2) growing number of angles at which the load can be observed continuously on the same ground target; and 3) progressive improvements in the spatial resolution of the payload. Fig. 1 shows polarized multiangle loads that have been launched

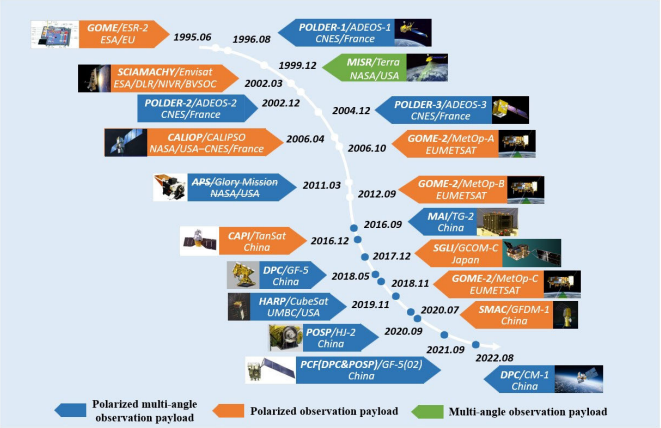

Fig. 1. Development status of polarized multiangle payloads (launched or completed missions).

or completed missions, the fairly typical of which are: Polarization and Anisotropy of Reflectance for Atmospheric Sciences coupled with Observations from a Lidar (PARASOL) of France and the China National Space Administration High-resolution Earth Observation System series of satellites, GaoFen-5 (GF-5). The POLarization and Directionality of the Earth's Reflectance-3 (POLDER-3) carried by PARASOL was developed based on POLDER-1 and POLDER-2. With POLDER-3, the number of observation angles of a ground target can be as high as 16; the central wavelengths of the polarization bands are 490, 670, and 865 nm; and the spatial resolution is 6 × 7 km at nadir [19], [20], [21].

Using the directional polarimetric camera (DPC) carried by GF-5 or GF-5(02), the number of observation angles can reach 12 and 17; the central wavelengths of the polarization bands are 490, 670, and 865 nm; and the spatial resolution increases to 3.3 km at nadir [20], [22]. Finally, the multiviewing, multichannel, multipolarization imager (3MI) developed by the European Space Agency is specifically designed for characterizing aerosols and clouds; the imager has undergone improvements as scientists anticipate incorporating it on the European Organisation for the Exploitation of Meteorological Satellites (EUMETSAT) Polar System-Second Generation (EPS-SG) platform from 2022 to 2040. With 3MI, the number of observation angles for a ground target is approximately 10–14 with nine polarization bands (the central wavelengths include 410, 443, 490, 555, 670, 865, 1370, 1650, and 2130 nm) [23], [24].

The continuous development of polarization multiangle payloads has led to enhanced performance and improvements in the accuracy of cloud characterization, mainly in the retrieval of parameters such as cloud masks, cloud optical thickness (COT), cloud top pressure, cloud top height, and cloud microphysical properties (cloud droplet size distribution, C-DSD, and cloud phase). Currently, the development of multiangle polarization payloads is rapidly advancing, and more satellite payloads will be launched in the future. For example, the Hyper-Angular Rainbow Polarimeter 2 (HARP2) developed by the University of Maryland/Baltimore County (UMBC) in the United States is to be launched by Pre-Aerosol, Clouds, and ocean Ecosystem mission (PACE) satellites on January 2024; National Aeronautics and Space Administration (NASA)'s Multi-Angle Imager for Aerosols (MAIAs) device was originally scheduled to launch in 2022 aboard the Orbital Test Bed (OTB)-2 spacecraft, which is now launching at a date to be determined; further examples include the American Spectro-Polarimetric Experiment One (SpexOne), the Ukrainian Scanning along track Polarimeter (ScanPol) and MultiSpectral Imaging Polarimeter (MSIP), and the European Union's Multi-Angle Polarimeter (MAP) [13], [25], [26], [27], [28], [29], [30].

Since POLDER is the first satellite payload in the world to combine multispectral with multipolarization and multiangle information, many remote sensing studies of cloud characteristics are based on POLDER data. Studies have shown that traditional single-view instruments cannot capture the instantaneous distribution of angular radiance [31], [32], [33], while polarized multiangle loads, such as POLDER, can provide almost synchronous bidirectional reflectance [34]. This has been proven to be useful for characterizing the angular variability of the reflectance of targets (aerosol, cloud, atmospheric water vapor content, and so on) and provides a better evaluative ability [35], [36]. The multiangle observation method also makes it possible to broaden the fixed cloud microphysical conditions and directly retrieve the single-scattering phase function [37], [38], [39]. Cheng et al. [40] found that multiangle polarization characteristics can be used to effectively identify the cloud phase and, subsequently, accurately distinguish between ice and water clouds. Bréon and Goloub [41] reported that, due to the polarized radiation characteristics of single scattering by cloud droplets, the POLDER-polarized light image exhibited cloud-bow characteristics in the scattering angle range of 150°–170°, indicating that the C-DSD has a narrow range and that POLDER's multiangle polarimetric measurements can allow for the accurate retrieval of the C-DSD. Through precise analysis, Chepfer et al. [42] concluded that the polarized reflectance is highly sensitive to the type of cirrus ice crystals in the scattering angle range of 60°–110°. In another study, Goloub et al. [43] showed that the angular polarization feature can be used to accurately distinguish between spherical and nonspherical particles, such as water and ice clouds, and provided a thorough analysis of the normalized polarized radiance as a function of the scattering angle. Di Girolamo et al. [44] noted that the distribution of plane-parallel clouds is closely related to the solar zenith angle and provided a reference for the conditions of considering ocean–water clouds as plane-parallel clouds through the combination of multiangle and multispectral information. Zeng et al. [45] analyzed the variation of the cloud cover observed by Moderate-Resolution Imaging Spectroradiometer (MODIS) and POLDER instruments using the satellite zenith angle and additionally found that different positions of the orbit, such as the edge and center of the swath, also affect the cloud cover observations. Alexandrov et al. [46] and Knobelspiesse et al. [47] studied the variation of the polarization characteristics of different types of clouds using the scattering angle to verify the sensitivity of multiangle polarization measurements to the optical characteristics of clouds; they proposed measuring the observed polarization cloud-bow features (scattering angle in the range of 135°–165°) and

applying the corresponding inverse transform to accurately retrieve the C-DSD via a parameter-free cloud-bow Fourier transform method. In another study, van Diedenhoven et al. [48] demonstrated the dependence of the single-scattering degree of linear polarization on the scattering angle, aspect ratio, and roughness of the hexagonal ice crystal model. Shang et al. [49] discovered that the use of a scattering angle in the range of 137°–165° rather than the range of 145°–165° in POLDER's official products for C-DSD retrievals can greatly reduce the uncertainty caused by cloud inhomogeneity. He et al. [50] conducted a sensitivity analysis by observing geometric parameters (the observation zenith, solar zenith, and relative azimuth angles) to reveal their influence on the optical properties of the top of the atmosphere. In summary, the observational geometric elements, such as the satellite orbit characteristics, scattering angle, and observation zenith angle, affect (whether directly or indirectly) the spectral and polarized radiation characteristics of clouds and are instrumental in the retrieval of cloud characteristics.

Studies have revealed that satellite observations differ from ground-based observations [51], [52]. Small changes in position lead to significant changes in the observational geometry because of the long distances from observation targets in satellite observations [19]. At the same time, the polarization characteristics of reflected light display high sensitivity to the observation angle [53]. However, no systematic analysis could be found in previous studies; thus, this article focuses on the influence of the observation angle and orbital position on cloud retrieval, and a systematic and detailed analysis is conducted to fill in the research gaps.

The variation in the polarized radiation characteristics of different cloud types with the scattering angle is simulated and the sensitivity of the former to the latter is systematically analyzed. On this basis, the observational data of three polarization multiangle loads of the POLDER-3, DPC/GF-5, and DPC/GF-5(02) sensors are investigated and the variation of the scattering angles and their values at different positions of the orbit is explored. In addition, the influences of the polarization multiangle observation payload orbit and observation angle on cloud characteristics retrieval are explored by considering the effective scattering angle range in the retrieval of cloud characteristics. This article strives to provide an effective reference for the development of multiangle, multipolarization, and multispectral satellite payloads and implementation of cloud retrieval. Section II describes the polarization multiangle observational dataset and analytical methods used here. Section III presents the main experimental results and discussion, including the influence of the scattering and on cloud retrieval and the investigation of the distribution law of the polarized multiangle load orbit scattering angle. In Section IV, a comprehensive scattering angle simulation and analytical model are proposed. Finally, Section V summarizes the main findings of the study.

II. Materials and Methods

A. POLDER Data

The POLDER-3 sensor, developed by Centre National d'Etudes Spatiales (CNES) and launched from a PARASOL satellite in September 2004, was used to analyze the characteristics of light reflected by the Earth and its atmosphere for nine years to better understand the role of clouds and aerosols in climate formation, with the observation mission ending in October 2013. The POLDER-3 sensor improved upon POLDER-1 and POLDER-2 sensors, which consists of three main components, namely, an array charge-coupled device (CCD) detector, a runner bearing a polarization and spectral filter, and a wide field-of-view telecentric optical path. The CCD detector matrix provides a spatial resolution of almost 6 km at the subsatellite point. When over a target, the POLDER-3 instrument can perform, from the solar radiation reflected by the target channel, nine spectral bands (with center wavelengths of 443, 490, 565, 670, 763, 765, 865, 810, and 1020 nm), and up to 16 consecutive multiangle observations. By adding a polarizer to the filter, the polarization information of the target for three of the nine spectral bands (with central wavelengths of 490, 670, and 865 nm) can be obtained. The polarization information is primarily described by the Stokes parameters I, Q, and U. The specific instrument characteristics of the POLDER-3 sensor are given in Table I [17], [35].

B. DPC Data

DPC, as China's first multiangle polarized Earth observation satellite sensor, is onboard the GF-5 satellite, which launched in May 2018 and is mainly used for the characterization of cloud and aerosol optical and physical information in the areas of atmospheric environmental monitoring and climate change research, where the high accuracy of atmospheric corrections of remote sensing data is critical. It provides a new perspective for future studies of the interaction between the Earth–atmosphere system and the cloud feedback mechanism. The GF-5 satellite is in a sun-synchronous orbit with an inclination of 98°, and the local transit time is 1:30 P.M. The DPC and POLDER-3 have nearly the same spectral and polarized observation band settings; the difference is that the band with a center wavelength of 1020 nm is canceled in the DPC. However, the nadir spatial resolution of DPC is 3.3 km, which is significantly improved compared with POLDER-3. The DPC can continuously capture, at a minimum, nine series of images with different observation angles for the same target on an orbit (with the specific instrument features shown in Table I. The GF-5(02) satellite with a DPC was also successfully launched in September 2021. Compared with DPC/GF-5, the number of observation angles was increased ($n \leq 17$), while the remaining parameters were unchanged [13], [15].

In this article, the primary data of DPC/GF-5 at 2 P.M. on March 2, 2020 and that of DPC/GF-5(02) at 2 P.M. on November 15, 2021 were selected for the experiment.

C. Principles of Multiangle Polarization Observation

The polarized state of light can be described by the four Stokes parameters I, Q, U, and V. However, elliptical polarization is rarely produced by sunlight reflected by natural

TABLE I
POLDER-3, DPC, HARP2, AND 3MI INSTRUMENT FEATURES

Categories	Specific characteristics			
Instrument/Satellite	POLDER-3/PARASOL	DPC/GF-5	HARP2/PACE	3MI/Metop-SG
Launch time(LT) or Estimated launch time(ELT)	2004.12 (LT)	2018.05 (LT)	2024.01 (ELT)	2022–2040 (ELT)
Spectral band/nm	443, 490, 565, 670, 763, 765, 865, 910, 1020	443, 490, 565, 670, 763, 765, 865, 910	441, 549, 669, 873	410, 443, 490, 555, 670, 763, 765, 865, 910, 1370, 1650, 2130
Polarization band/nm	490, 670, 865	490, 670, 865	441, 549, 669, 873	410, 443, 490, 555, 670, 865, 1370, 1650, 2130
FWHM/nm	13.5, 16.5, 15.5, 15.0, 11.0, 38.0, 33.5, 21.0, 17.0	20, 20, 20, 20,10, 40, 40, 20	15, 12, 16, 43	20, 20, 20, 20, 20, 10, 40, 40, 20, 40, 40, 40
FOV	Along track ± 51°, across track ± 43°	Along track/across track ± 50°	Along track ± 57°, across track ± 47°	Along track/across track ± 51°
Number of observation directions	$n \leq 16$	$9 \leq n \leq 12$	10 angles at 441, 549, and 873 nm; 60 angles at 669 nm	$14 \leq n \leq 21$
Spatial resolution	Nadir 5.3 km × 6.2 km	Nadir 3.3 km	Nadir < 3 km	Nadir 4 km
Satellite track height	705 km	705 km	676 km	835 km
Satellite track type	Sun-synchronous orbit			
Swath	2100 × 1600 km^2	1850 × 1850 km^2	——	2200 × 2200 km^2

surfaces and scattered by the atmosphere; thus, the parameter V is sufficiently small to be negligible relative to the remaining three parameters. Both POLDER-3 and the DPC have three polarized bands (490, 670, and 865 nm), each of which contains three polarized channels (0°, 60°, and 120°). By combining the three polarized channels, the Stokes vectors I, Q, and U of the top-of-the-atmosphere electromagnetic field in the satellite sensor field of view can be obtained, and the observed values of these vectors can be used to invert the atmospheric parameters. For each polarization band of the multiangle polarization load, the radiometric values of the three polarization channels (0°, 60°, and 120°) are denoted as L_1–L_3, respectively, from which the expressions in the following equation can be obtained:

$$\begin{cases} L'_n = \dfrac{2}{3}(L_1 + L_2 + L_3) \\ L'_{np} = \dfrac{4}{3}\sqrt{L_1^2 + L_2^2 + L_3^2 - L_1L_2 - L_2L_3 - L_1L_3} \end{cases} \tag{1}$$

where L'_n is the total incident emissivity and L'_{np} is the polarization emissivity. Equation (1) can be rewritten by assuming that there is linearly polarized light in the detector direction and defining $S_0 = 2(L_1+L_2+L_3)/3$, $S_1 = 2(2L_1-L_2-L_3)/\sqrt{3}$, $S_2 = 2(L_2-L_3)/\sqrt{3}$, and $S_3 = 0$; in this way, the relation $L'_n = S_0$ and $L'_{np} = (S_1^2 + S_2^2)^{1/2}$ can be used [22].

Polarized multiangle loads are often characterized by the normalized reflectance L_n, and the normalized emissivity L_n is equal to the product of the reflectance R of the surface of the atmospheric system and the cosine of the solar zenith angle $\mu_0(\cos\theta_0)$, as shown in the following equation:

$$L_n(\mu, \mu_0, \varphi, \varphi_0) = \mu_0 R(\mu, \mu_0, \varphi, \varphi_0). \tag{2}$$

The reflectance R can be calculated as shown in the following equation:

$$R(\mu, \mu_0, \varphi, \varphi_0) = \frac{\pi I(\mu, \mu_0, \varphi, \varphi_0)}{E_0\mu_0} \tag{3}$$

where $I(\mu, \mu_0, \varphi, \varphi_0)$ is the emissivity and $E_0\mu_0$ is the irradiance of incident unpolarized light (or solar irradiance). Similarly, the polarization reflectance is defined in terms of the normalized polarization emissivity; in other words, the normalized polarization emissivity $L_{np} = (Q^2 + U^2)^{1/2}$ is equal to the polarization reflectance R multiplied by μ_0 [54], as given by the following equation:

$$\begin{aligned} L_{np}(\mu, \mu_0, \varphi, \varphi_0) &= \mu_0 R_p(\mu, \mu_0, \varphi, \varphi_0) \\ &= \frac{\pi\sqrt{Q_i^2 + U_i^2}}{E_0}. \end{aligned} \tag{4}$$

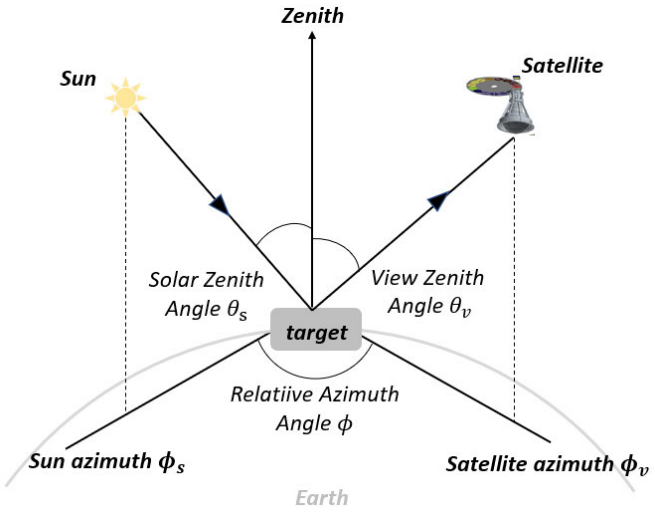

Fig. 2. Schematic of positions of different angles in satellite observation geometry.

In this article, the polarization reflectance and the polarization phase function are used to show the sensitivity of the cloud polarization radiation characteristics to the scattering angle.

D. Satellite Observation Geometry and Scattering Angle

The observation geometry of a satellite is a solid geometric figure formed by the incident light from the Sun, the reflected light received by the satellite sensor, the target, and the satellite sensor when the satellite is observed. It includes the following angle parameters: the solar zenith angle θ_0, view zenith angle θ_v, solar azimuth angle ϕ_0, view azimuth angle ϕ_v, relative azimuth angle ϕ, and scattering angle Θ. Usually, geometric parameters of satellite observations other than the scattering angle are included in the observation data. The positions of the angles in the observation geometry of a satellite are given in Fig. 2.

The angle between the incident light and the scattered light is called the scattering angle, which is significant in the process of cloud retrieval. The effective scattering angle range can provide important information for the retrieval of different cloud parameters. The scattering angle can be calculated as shown in the following equation:

$$\begin{aligned}\cos\Theta &= \cos\theta_0 \times \cos\theta_v + \sin\theta_0 \times \sin\theta_v \times cos\phi \\ &= \mu\mu' + \sqrt{(1-\mu^2)(1-\mu'^2)}\cos\phi. \end{aligned} \tag{5}$$

The experimental process used in this article is shown in Fig. 3, which is divided into three main parts. The first part focuses on simulating the variations in polarized radiative properties of liquid water cloud and ice cloud with different scattering angles using the ARTDECO radiative transfer model. In addition, it analyzes the sensitivity of these properties to scattering angles. In the second part, based on the observations of three polarized multiangle loads [POLDER-3/PARASOL, DPC/GF-5, and DPC/GF-5(02)], the distribution of scattering angles, scattering angle ranges, and scattering angle densities for their whole orbits and six local representative regions is calculated, counted, and analyzed. The first two parts are both performed in connection with the effective scattering angle ranges of five cloud parameters retrieval summarized in Section III-A. Finally, in the third part, we develop a comprehensive analytical model for evaluating the validity of load scattering angles in retrieval of different cloud parameters, with a view to providing a reference for the development of polarized multiangle payloads.

III. Results

A. Sensitivity Analysis of Cloud Polarization Radiation Characteristics

The scattering angle holds significant importance in cloud retrieval as it is utilized in a wide range of cloud parameter retrieval algorithms. Whether directly or indirectly, the scattering angle or its range is incorporated into the majority of these algorithms to ensure precise and reliable results. The effective scattering angle range can provide easily resolved information for cloud characteristics retrieval. The sensitivity of the polarized radiative properties (polarized phase function and polarized reflectivity) of liquid water clouds and ice clouds to the scattering angle is first analyzed based on the ARTDECO radiative transfer model in conjunction with the effective scattering angle range of cloud parameter inversion.

1) Polarized Phase Function to Scattering Angle: The response of the polarization phase function of liquid water cloud droplets with different effective radii and variances to the scattering angle at 865 nm was simulated using the Mie scattering theory. For the simulation of ice clouds, we use the inhomogeneous hexagonal monocrystal (IHM) model as the basic shape of ice crystal particles [55], [56]. The IHM model defines ice crystals as hexagonal prisms with bubbles or aerosol particles inside, and the bubbles or aerosols obey a standard Γ-distribution, whose exact form is determined by the effective radius r_{eff}, and the effective variance (EV) v_{eff}. The propagation of light on the surface and inside of ice crystals is calculated by geometrical optics methods, Monte Carlo theory, and Mie scattering theory. The shape of the IHM is defined by the aspect ratio $Q(L/2R)$, where L is the height of the hexagonal prism and R is the radius of the base of the hexagonal prism, and the size of the IHM is expressed by the radius R_v of the equivalent spherical volume. Also, the mean free path length $\langle \ell \rangle$ indicates the random distribution of bubbles or aerosol particles in the ice crystal particles. In this article, the ice crystal hexagonal prism is set to contain only air bubbles in the simulation. The simulation results are shown in Figs. 4–6.

By consulting relevant literature and data, the effective scattering angle ranges corresponding to the retrieval of four common cloud parameters are obtained as follows: 1) C-DSD: 135°–165°; 2) cloud phase 1 (C-Phase1): 60°–120° and cloud phase 2 (C-Phase2): 80°–165°; 3) cloud ray pressure (C-RayPressure), 80°–120°; 4) 443-nm band cloud detection [C-Det(443 nm)]: 80°–120°; and 5) 865-nm band C-Det [C-Det(865 nm)]: 135°–150°. These are shown in Table II and the corresponding positions are shown in Figs. 4, 5 and 6.

Fig. 4(a)–(d) shows the variation of polarized phase function with scattering angle corresponding to different effective radii

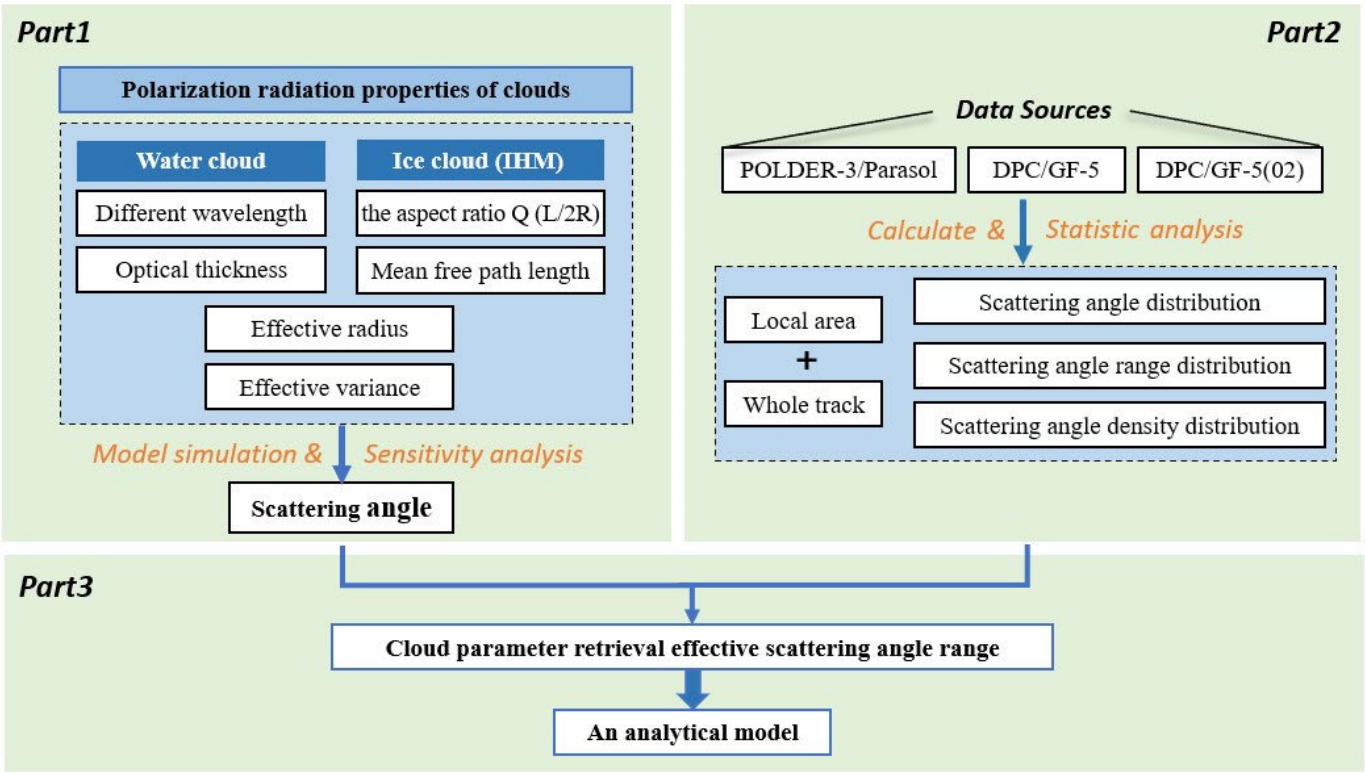

Fig. 3. Experimental flowchart.

TABLE II
EFFECTIVE SCATTERING ANGLE INTERVAL FOR RETRIEVAL OF COMMON CLOUD PARAMETERS

Cloud parameter	Effective scattering angle range	Sensor/Satellite (data source)	Citation
Cloud droplet size distribution	150°~170°	POLDER-1/ADEOS-I	Bréon, F. M., & Goloub, P. 1998
	142°, 145°~165°	POLDER-2/ADEOS-II	Bréon, F. M., & Doutriaux-Boucher, M. 2005
	135°~165°	RSP–airborne prototype for APS	Alexandrov, M. D., et al. 2012
	137°~165°	POLDER-3/PARASOL	Shang, H., et al. 2015; Shang, H., et al. 2019
	135°~160°	LES–satellite retrieval simulator, AirMSPI	Miller, D. J., et al. 2018 Xu, Feng, et al. 2018
Cloud phase	0°~150°	AVHRR	Key & Intrieri 2000
	60°~140° (865 nm) Around 140° (865 nm) 140°~180° (865 nm)	POLDER-1/ADEOS-I	Goloub et al. 2000
	90°~145°	POLDER-3/PARASOL	Riedi et al. 2010
	80°~165°	DPC/GF-5	Shang, H., et al. 2020
Cloud Rayleigh pressure	80°~120° (443 nm)	POLDER-2/ADEOS-II	Vanbauce, C. 2003
Cloud detection	80°~120° (443 nm) 135°~150° (865 nm)	POLDER-3/PARASOL; DPC/GF-5	Buriez, J. C., et al. 1997; Li, Chao et al. 2019

(CER) of liquid water cloud droplets for EV of 0.01, 0.03, 0.09, and 0.29, respectively. When the EV is constant, the polarization phase function curves of cloud droplets with different effective radii almost coincide in the scattering angle

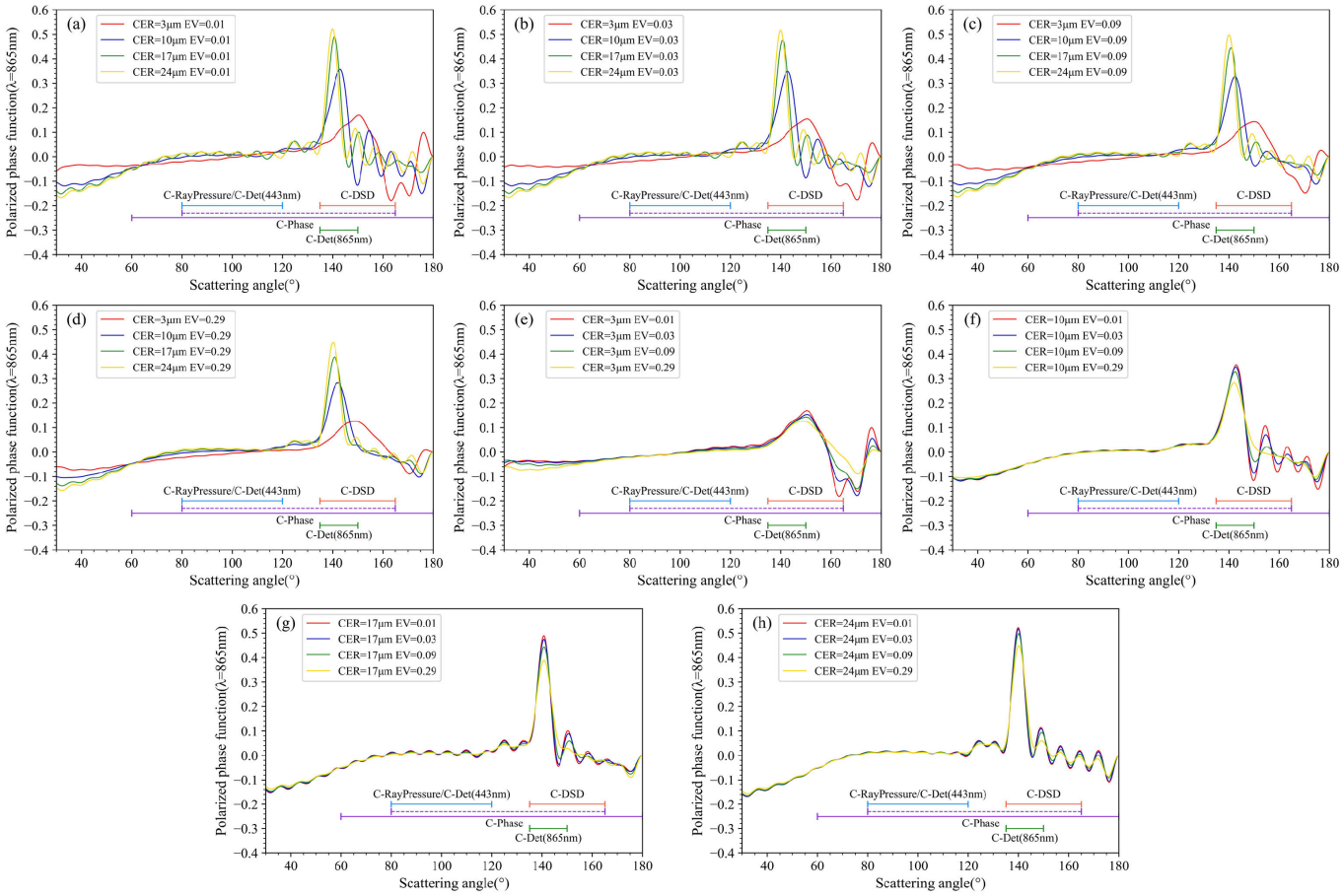

Fig. 4. Variation of polarization phase function corresponding to different water cloud parameters with the scattering angle. (a) EV = 0.01, (b) EV = 0.03, (c) EV = 0.09, (d) EV = 0.29, (e) CER = 3 μm, (f) CER = 10 μm, (g) CER = 17 μm, and (h) CER = 24 μm.

range of 30°–130°, but the polarization phase function curves fluctuate more in the scattering angle range of 130°–180°. With the increase of the effective radius of the cloud droplets, the fluctuation range of the polarization phase function is widened and the degree of fluctuation is more intense.

As shown in Fig. 4(a), the polarized phase function fluctuation range is between −0.2 and 0.15 when the CER is 3 μm, and then, the band range increases from −0.1 to 0.5 when the CER increases to 24 μm. With the increase of CER, the scattering angle corresponding to the first peak of the polarization phase function curve is gradually shifted to the left, and the first peaks of the curve appear at 150°, 142°, 141°, and 140° for CER of 3, 10, 17, and 24 μm, respectively. It can be seen that when the EV value is 0.01, the curve has four peaks in the scattering angle range of 130°–180°, and the first peak is located around 140°, which is called the "first rainbow." When the EV value is 0.01, 0.03, and 0.09, the fluctuation ranges of the polarized phase function are −0.12 to 0.1, −0.1 to 0.1, and −0.09 to 0.09, respectively, while when the EV value is 0.29, the fluctuation ranges are only −0.09 to 0.06, i.e., the fluctuation ranges are gradually decreasing with the increase of EV value.

Fig. 4(e)–(h) shows the variation of the polarized phase function with the scattering angle corresponding to the value of EV when the effective radius of the liquid water cloud droplet is 3, 10, 17, and 24 μm, respectively. When the CER is small, the effect of EV on the polarized phase function is large; with the increase of CER, the polarized phase function curves for different EVs converge. In addition, the fluctuation of the curves decreases with the increase of EV. For example, in Fig. 4(f), when the CER is 10 μm, the polarized phase function curves with EV of 0.01 show eight peaks in the scattering angle range of 130°–180°. However, when the EV value is increased to 0.29, the polarized phase function curve shows only two peaks in the same scattering angle range, and the range of fluctuation is smaller than that of the EV value of 0.01.

Fig. 4 indicates that the effective scattering angle range can provide richer information for the retrieval of cloud parameters. Considering the C-DSD as an example, in the scattering range of 137°–165°, the variations between liquid water clouds of different CERs and EVs can be notably identified. This significantly improves the efficiency and effect of the cloud parameter retrieval algorithm and greatly benefits the retrieval of cloud characteristics.

The simulation results of the ice clouds are shown in Fig. 5, and it is easy to find that the polarized phase function of ice cloud has two obvious peaks mainly at the scattering angles of 22° and 46°, which are the common 22° halo and 46° halo. The peak of the 22° halo decreases with the gradual increase

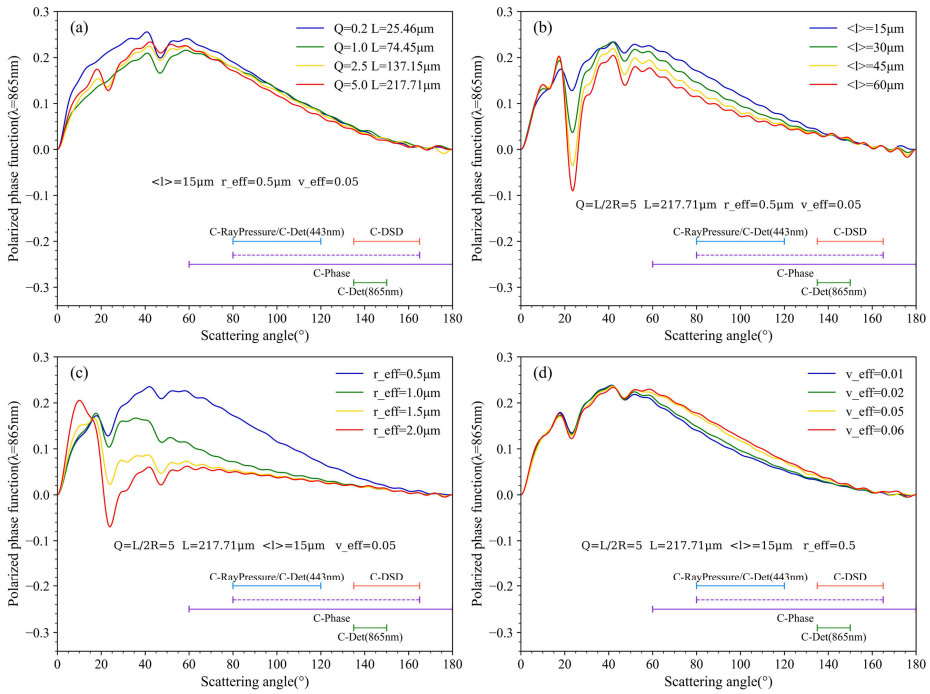

Fig. 5. Variation of polarized phase function corresponding to different ice cloud parameters with the scattering angle. Parameters varied are (a) aspect ratio Q, (b) mean free path $\langle \ell \rangle$, (c) effective radius r_{eff}, and (d) EV v_{eff}. When changing one parameter, the other parameters remain unchanged.

of Q, $\langle \ell \rangle$, r_{eff}, and v_{eff} parameters. In addition, it can be found that $\langle \ell \rangle$ and r_{eff} have a greater influence on the polarized phase function, which changes more significantly with the variation of these two parameters. Compared with water clouds, the variation of the polarized phase function with scattering angle for ice clouds is relatively less pronounced.

2) Polarized Reflectivity to Scattering Angle: Under the conditions of $\lambda = 0.490$, 0.670, and 0.865 μm, cloud droplets with different effective radii and COT values are selected to analyze the variation rule of the normalized polarized reflectivity of cloud droplets with scattering angle. The method for calculating the normalized polarized reflectance was described in Section III-A. Fig. 6(a), (c), and (e) shows that under the condition of a constant optical thickness, the normalized polarized reflectivities of water cloud droplets with varying effective radii are markedly distinct in the scattering angle range of 135°–155°. As the wavelength decreases, the normalized reflectance of the effective radii of water cloud droplets tends to be consistent. Considering the case where $\lambda = 0.490$ μm and COT $= 1$, in the scattering angle range of 135°–155°, the peaks of the normalized polarized reflectance of cloud droplets with a CER of 5, 10, 20, and 30 μm appear at 142°, 142°, 139°, and 139°, respectively, and the peak value increases gradually from 0.04 to 0.06. When the CER is held constant, barring the normalized polarized reflectance of cloud droplets with different optical thicknesses in the scattering angle range from 120° to 135°, which is nearly equal, dissimilarities occur in other regions of the curves. For scattering angles less than 120°, the normalized reflectance decreases with increasing optical thickness, and for angles greater than 135°, the normalized reflectance increases with increasing optical thickness. The same is true for the normalized reflectance curves with wavelengths of 0.670 and 0.865 μm. As can be seen from Fig. 6(g)–(i), the normalized polarization phase functions of the ice clouds do not show large differences.

B. Scattering Angle Distribution in the Whole Track

Based on the observation geometry of the satellite—the observed zenith, solar zenith, and relative azimuth angles of the whole orbit data of the POLDER-3/PARASOL, DPC/GF-5, and DPC/GF-5(02) loads—the scattering angle for each pixel is extrapolated. The angle data of these three sensors have 14, 12, and 17 layers, respectively. Calculations and statistical analysis revealed that although the multiangle polarization load data exhibit scattering in each layer, the angular distribution is slightly different, while the general distribution remains the same. Furthermore, with the continuous increase in the number of layers, the effective value of the observation angle continues to decrease; thus, the ninth, fifth, and fourth layers of data were randomly selected for analysis. The second layer of the whole orbit scattering angle distribution of the POLDER-3/PARASOL, DPC/GF-5, and DPC/GF-5(02) systems is shown in Fig. 7.

From the scattering angle distribution of the entire POLDER-3 orbit, the higher scattering angles are mostly distributed at low latitudes, and the scattering angles near the equator are mostly between 80° and 180°, that is, the scattering angle gradually decreases from 80° to 180° near the equator to 20° with increasing latitude. At the same time, the track color gradually warms from cooler to warmer as it moves from east to west, that is, the scattering angle of the east side of the POLDER orbit is generally smaller than that of the west side, and the scattering angle of the east side of the

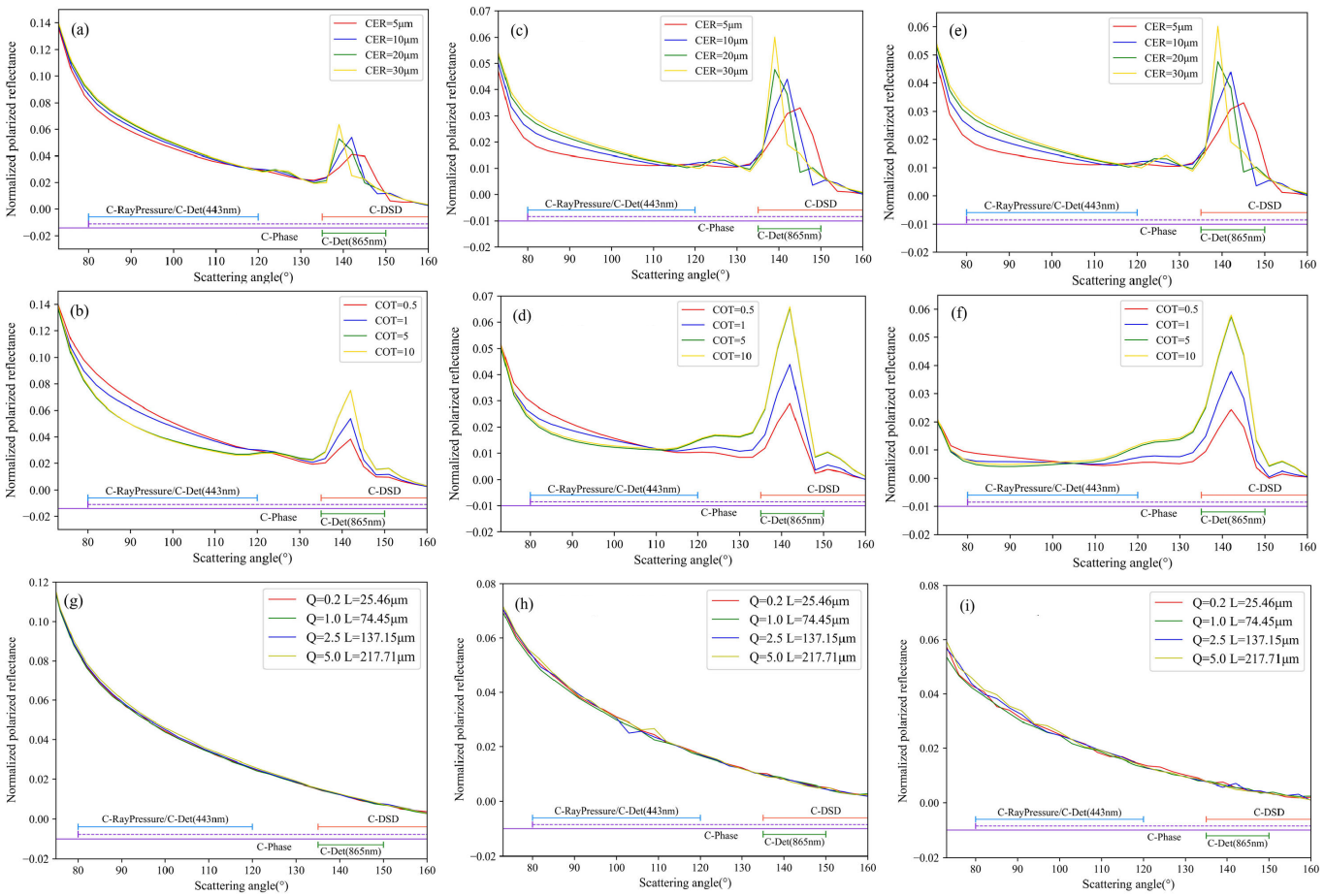

Fig. 6. Variation of polarization reflectance of cloud droplets with different effective radii and optical thicknesses as a function of the scattering angle. (a)–(f) Simulation results of water clouds. (g)–(i) Ice clouds results.

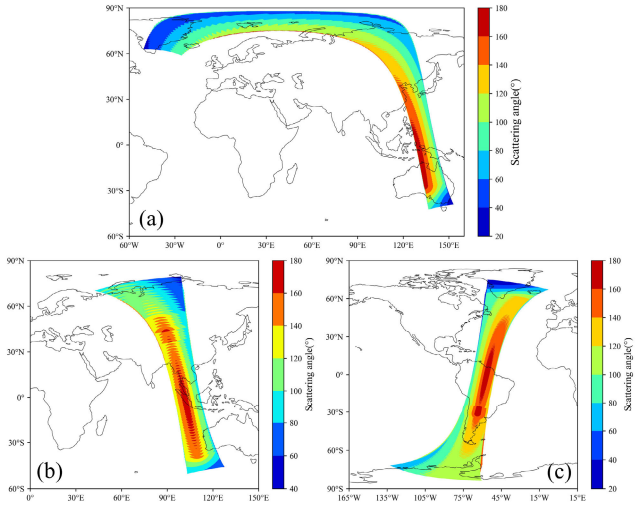

Fig. 7. Scattering angle distribution of the whole orbit of (a) POLDER-3/PARASOL on July 26, 2013, (b) DPC/GF-5 on March 2, 2020, and (c) DPC/GF-5(02) on November 15, 2021.

orbit is mainly concentrated in the range of 0°–100°, while the scattering angle of the west side of the orbit is mainly concentrated in the range of 100°–180°.

The scattering angle distribution of the whole orbit of DPC is similar to that of POLDER-3. The scattering angle decreases from the center of the orbit to the north, south, and east sides of the orbit and increases toward the west side of the orbit, and the scattering angle above 140° is mainly distributed in the equatorial region of the west side of the orbit (more than 60°). The scattering angle distribution pattern of the whole orbit of DPC(02) is slightly different, and the distribution of the north–south scattering angle is the same as that of POLDER-3 and DPC, but the distribution of the east–west scattering angle is opposite to the former two. The north–south scattering angle distribution is the same as that of POLDER-3 and DPC, but the east–west scattering angle distribution is opposite to the first two.

C. Distribution of Scattering Angle Range in Local Areas

Based on the analysis of the approximate distribution of scattering angles, six representative rectangular areas with greater cloud cover were selected on the three polarized multiangle load orbits: NW, in the west of the northern high-latitude area; NE, the eastern side in the northern high-latitude area; SW, on the west side of the southern high-latitude region; SE, on the east side of the southern high-latitude region; TW, on the west side of the equatorial region; and TE, on the east side of the equatorial region. The specific latitude and longitude ranges are shown in Table III.

TABLE III
LATITUDE AND LONGITUDE RANGES OF SELECTED REGIONS ON POLARIZATION MULTIANGLE LOAD TRACK

Polarized multi-angle payload	Serial number	Code	Latitude range	Longitude range
POLDER-3/ PARASOL	a	NW	70°N~80°N	90°E~105°E
	b	NE	70°N~80°N	110°E~135°E
	c	TW	10°N~10°S	125°E~130°E
	d	TE	10°N~10°S	137°E~142°E
	e	SW	45°S~35°S	135°E~142°E
	f	SE	45°S~35°S	148°E~155°E
DPC/GF-5	a	NW	50°N~60°N	70°E~80°E
	b	NE	50°N~60°N	92°E~102°E
	c	TW	10°N~10°S	95°E~100°E
	d	TE	10°N~10°S	105°E~110°E
	e	SW	40°S~50°S	100°E~110°E
	f	SE	40°S~50°S	115°E~125°E
DPC/GF-5(02)	a	NW	30°N~40°N	55°W~65°W
	b	NE	30°N~40°N	40°W~50°W
	c	TW	10°N~10°S	63°W~70°W
	d	TE	10°N~10°S	50°W~57°W
	e	SW	50°S~60°S	80°W~90°W
	f	SE	50°S~60°S	60°W~70°W

1) POLDER-3/PARASOL: The distribution of the six selected rectangle areas on the POLDER-3/PARASOL track is shown in Fig. 8(g). For each pixel, the multidirectional acquisition method of the polarization multiangle sensor provides multiple views distributed between the minimum and maximum values, that is, different observation angles. The scattering angles can be calculated from the observation angles. By extracting the maximum and minimum values of all scattering angles for each pixel, the scattering angle range of a pixel is obtained. The distribution of the scattering angle range of the selected areas is shown in Fig. 8(a)–(f). The minimum value of all scattering angles of each pixel is used as the horizontal axis coordinate, and the maximum value is used as the vertical axis coordinate. The colorbar represents the color codes based on the number of points, and the blue line segment, representing the case where the maximum and minimum values are equal (1:1 diagonal), indicates the corresponding position of the scattering angle of a single-view sensor.

From Fig. 8, it can be seen that the scattering angle and scattering angle range of area c (TW) are the largest, which are larger than those of area a (NW) and area e (SW); meanwhile, the scattering angles of area b (NE) and area f (SE) are also lower than those of area d (TE). Longitudinally, the scattering angles of regions b, d, and f are overall smaller than those of the left three regions at the same latitude and the range of scattering angles.

2) DPC/GF-5: The distribution of the six selected rectangular areas on the DPC/GF-5 track is shown in Fig. 9(g), and that of the scattering angle range in the selected areas is shown in Fig. 9(a)–(f).

Fig. 9 shows that the scattering angle ranges corresponding to the four high-latitude regions a, b, e, and f are lower than those of the two regions c and d near the equator, highlighting the advantages of polarization, multiangle loading, and multidirectional information. In addition, the maximum scattering angles are about 80°–180° for regions a, c, and e, around 60°–160° for regions d and f, and 100°–160° for region b. The maximum scattering angles for the regions around the equator are around 60°–160°. The maximum scattering angles are significantly higher around the equator than at higher latitudes and are about 20° higher in regions b, d, and f in the western region than in the eastern region.

3) DPC/GF-5(02): The six regions of the DPC/GF-5(02) load track are the same as those of POLDER-3 and the DPC, as shown in Fig. 10(g). Similar to the previous two sensors, the scattering angle range for high-latitude regions is smaller compared to the low-latitude equatorial regions, and the maximum scattering angle is also smaller. Scattering angle and overall scattering angle range on east side of DPC/GF-5(02) track are smaller than those on the west side.

To clarify the results and facilitate their comparison, the range of scattering angles in six regions of the orbit of the three multiangle polarized payloads is shown in the form of histograms, as shown in Fig. 11. The scattering angles of the high-latitude regions are lower than those of the low-latitude regions, and the relative situation of the scattering angles on the east and west sides of the orbits is clearer in

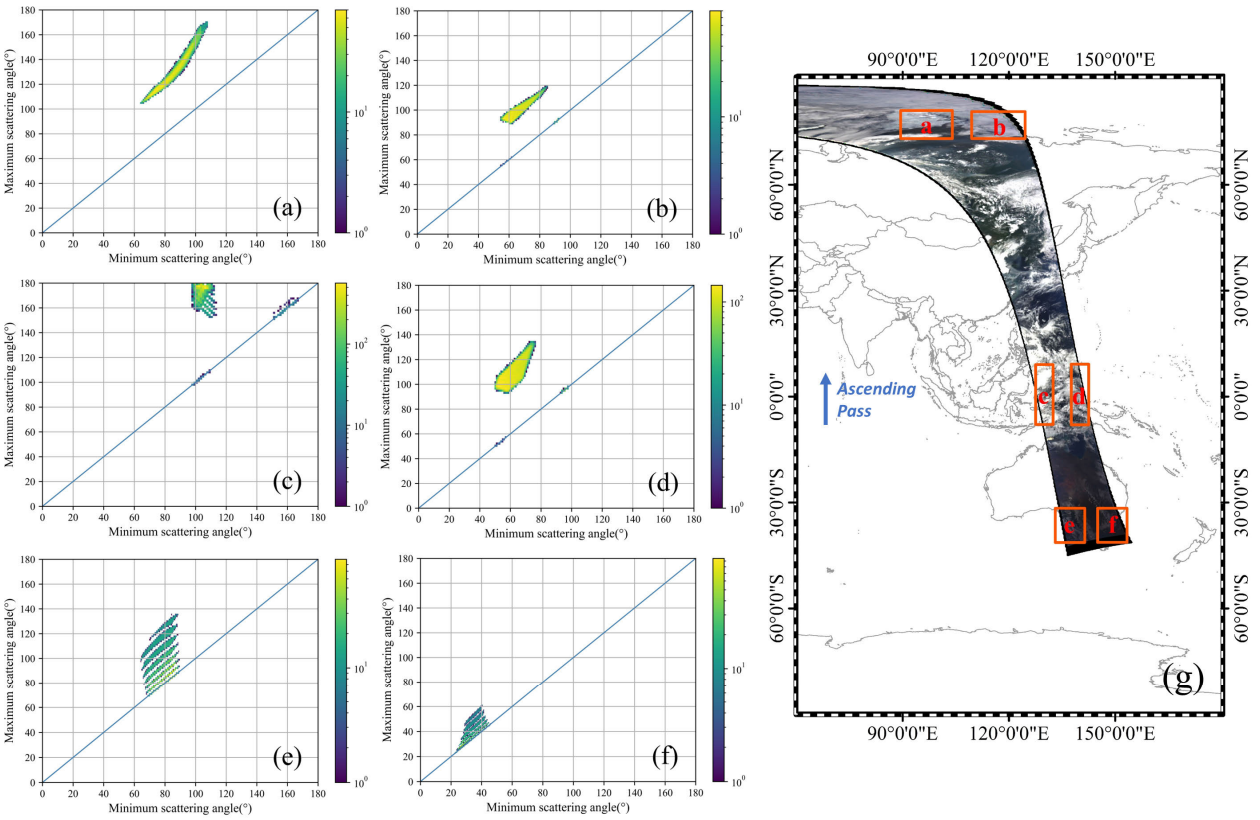

Fig. 8. Distribution of selected regions and their scattering angle ranges for the POLDER-3/PARASOL orbit on July 26, 2013.

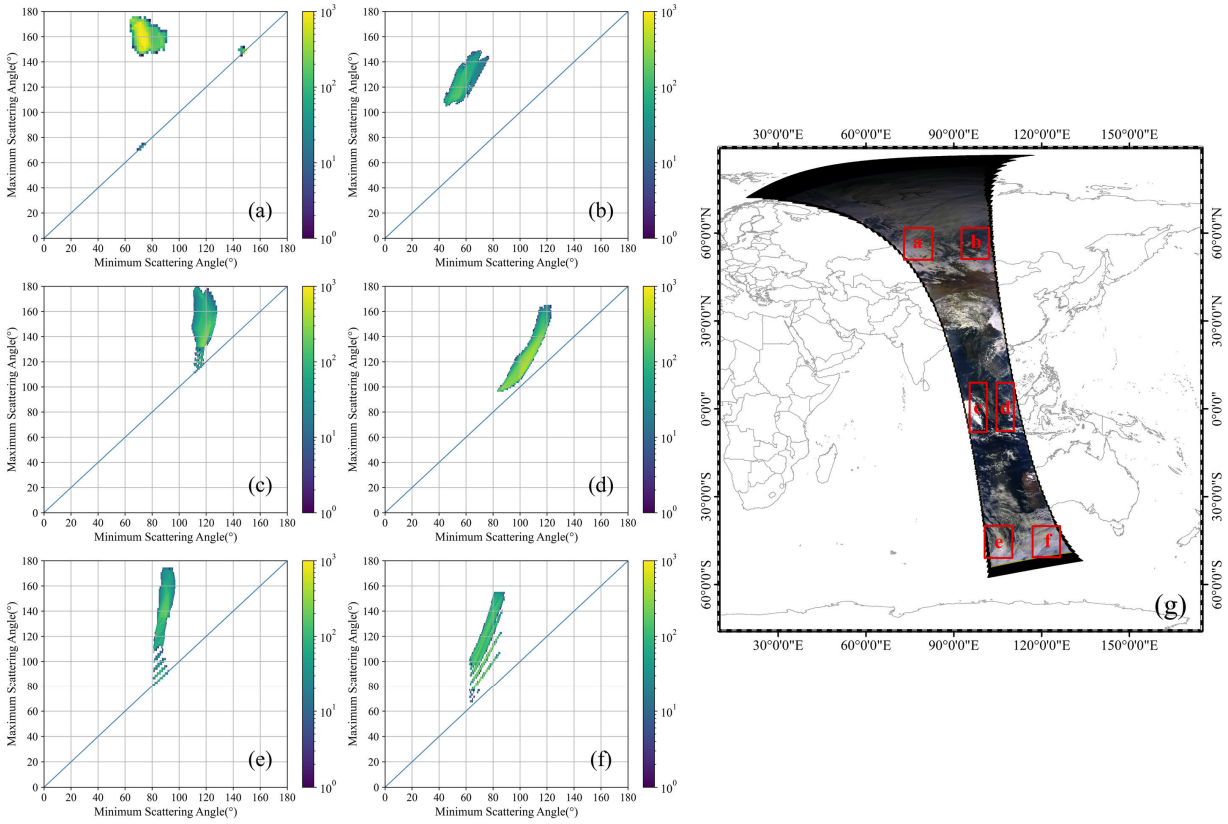

Fig. 9. Distribution of the selected regions and their scattering angle ranges for the DPC/GF-5 orbit on March 2, 2020.

larger areas. The multidirectional acquisition method of the multiangle polarization load entails a significantly larger range of scattering angles than that of the unidirectional acquisition method. The richness of the angle information is maximized,

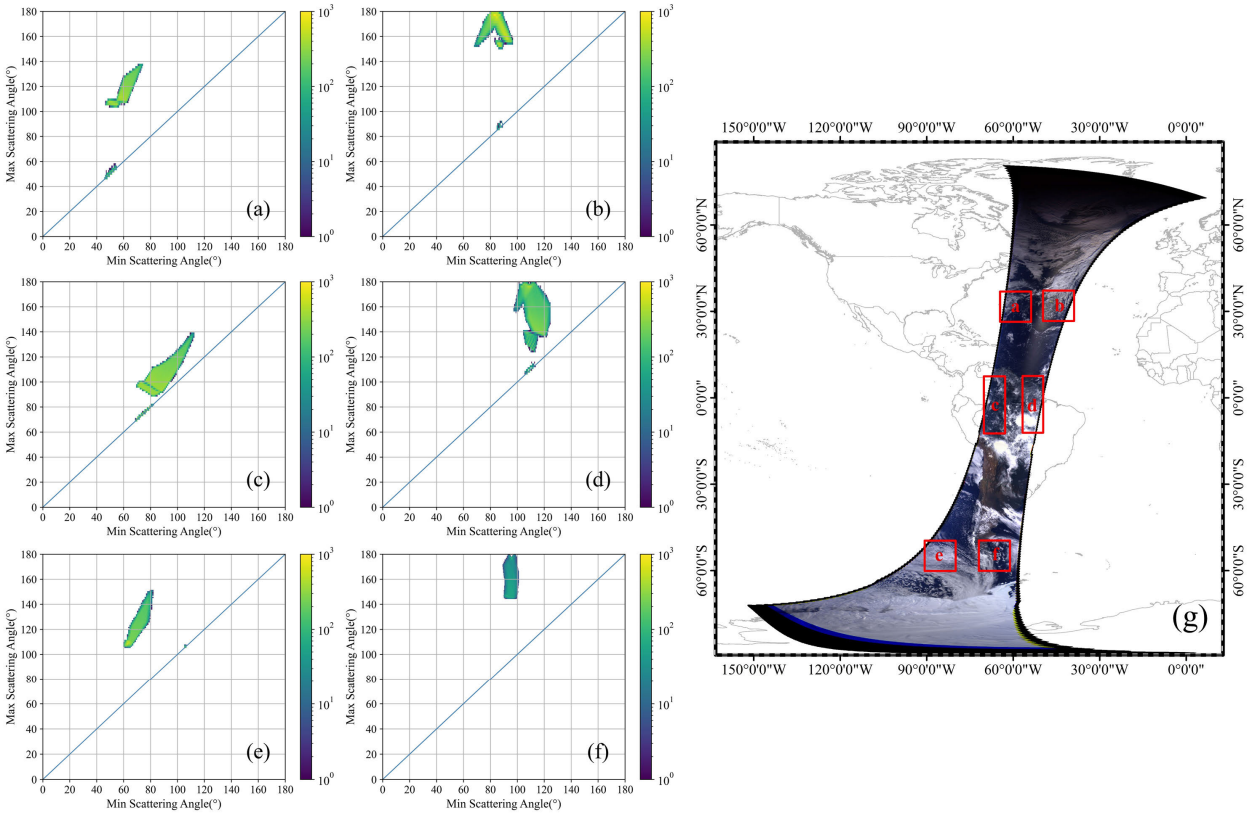

Fig. 10. Distribution of the selected regions and their scattering angle ranges for the DPC/GF-5(02) orbit on November 15, 2021. (a)–(f) Six selected local regions NW, NE, TW, TE, SW, and SE, respectively. (g) Distribution of the six regions in the whole track.

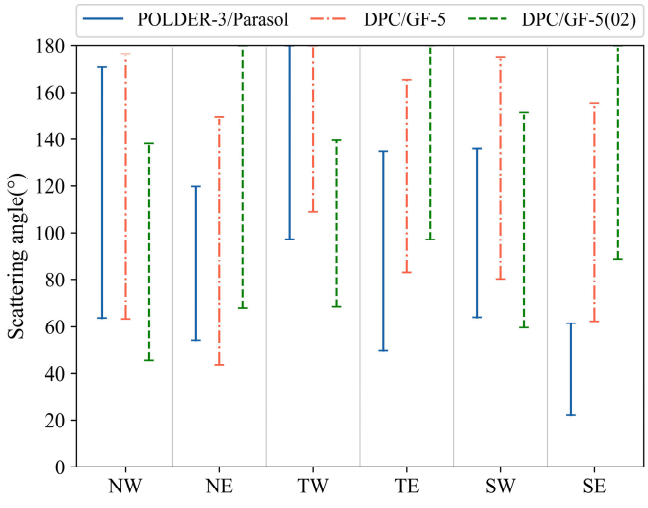

Fig. 11. Comparison of scattering angle distribution in the selected regions of multiangle polarization load orbits.

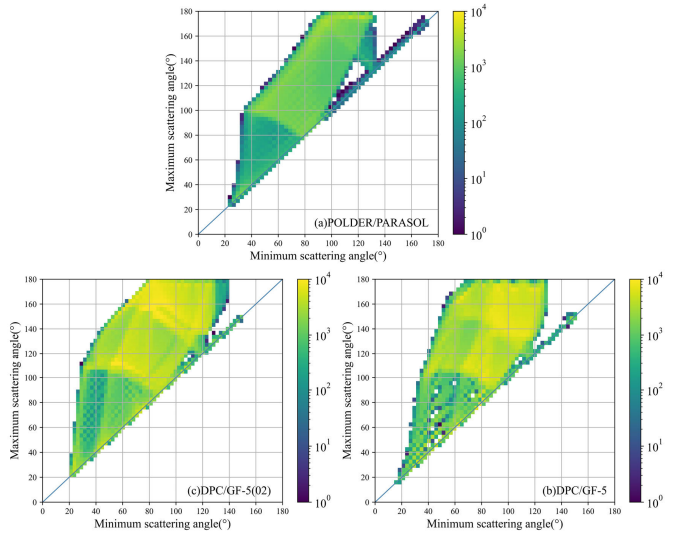

Fig. 12. Distribution of the whole orbit scattering angle range under polarization multiangle loads.

and the collected cloud characteristics are more accurate and display enhanced retrieval accuracy.

D. Distribution of the Whole Orbit Scattering Angle Range

The distribution of the scattering angle range of the whole orbits of the three multiangle polarization loads of POLDER-3/PARASOL, DPC/GF-5, and DPC/GF-5(02) was statistically analyzed in this article, as shown in Fig. 12.

The whole orbit scattering angle distributions of the three loads reveal that the scattering angle range of the whole orbits of POLDER-3, DPC(02), and DPC is distributed between 20° and 160°. However, regarding the number of scattering angles, that of the entire orbit of DPC and DPC(02) is greater than the total number for POLDER. In addition, the upper left corner of the scattering region has the largest range of scattering angles, mostly between 80° and 180°, and this type

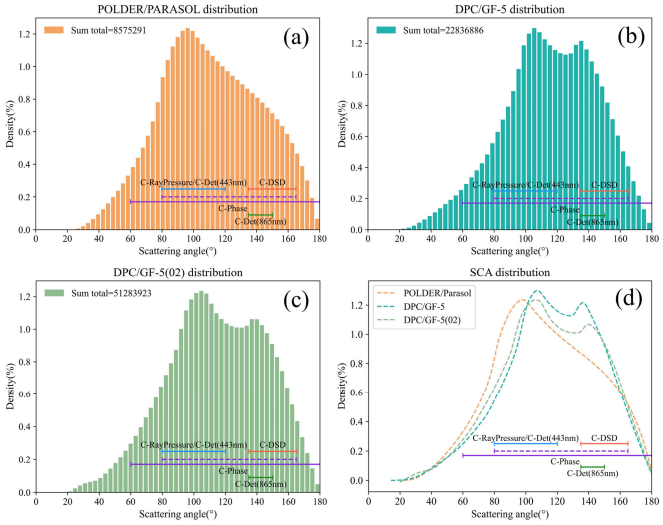

Fig. 13. Histograms of the whole-track scattering angle density distributions of polarized multiangle loads. (a) POLDER-3/Parasol. (b) DPC/GF-5. (c) DPC/GF-5(02). (d) Whole-track scattering angular density distribution curves of the three loads.

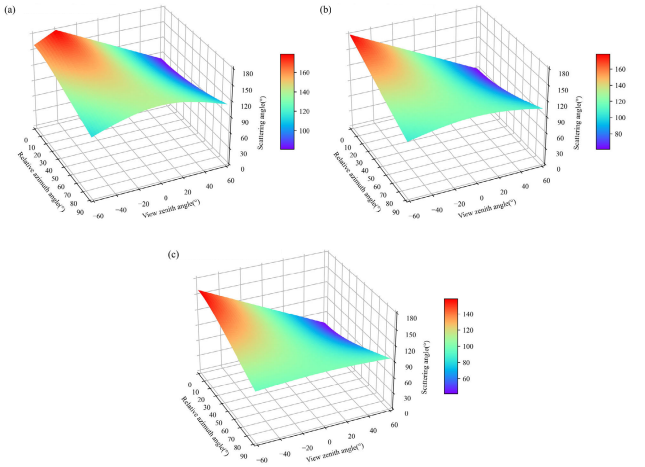

Fig. 14. Scattering angle simulation results. (a) Solar zenith angle = 40°. (b) Solar zenith angle = 60°. (c) Solar zenith angle = 80°.

of region maximizes the acquisition of multiangle information. According to the analysis in Section III-A, such regions tend to be located at the center of low-latitude orbits.

In the cloud characteristics retrieval algorithm, not only is the specific angle range crucial to the parameter retrieval accuracy and results, but the angle distribution density within the specific range also influences retrieval result. The angle distribution density was statistically analyzed, as shown in Fig. 13. Within the effective range of scattering angles for C-Phase, C-DSD, and C-Det (865 nm), those of DPC and DPC(02) are significantly higher than that of POLDER-3 However, it is not difficult to see that due to the fact that the total number of angles of DPC/GF-5(02) is higher than that of DPC, even though the density distributions of DPC and DPC(02) are approximate, and even if the density distribution of DPC is slightly higher than that of DPC(02) at the peak, the number of scattering angles in the effective scattering angle inversion range of DPC(02) is still higher than that of DPC.

Statistical analysis revealed that the total number of scattering angles of the entire orbit of DPC(02) is 51 283 923, which is significantly higher than that of POLDER-3 (8 575 291) and DPC (22 836 886). This is because the maximum number of observable angles of DPC(02) can reach up to 17, while the maximum number of observable angles of POLDER-3 and DPC is 16 and 12, respectively. The higher the number of observation angles, the greater the number of scattering angles in the whole orbit. Within a given range, the distribution density of load angles increases as the number of observation angles increases.

IV. Analytical Model

In the process of observation evaluation of satellite payload design, one of the first problems to be solved is whether the target observation area is within the range that can be covered by observation during satellite operation, and when the target observation area is adjusted to the range that can be covered by the satellite according to the time and the satellite orbital parameter, then the evaluation of the effectiveness of the cloud parameter retrieval observation in the study can be carried out. The time and satellite orbit parameters are used as inputs to calculate the relative azimuths of solar information (solar zenith angle and solar azimuth) and satellite information (satellite zenith angle and satellite azimuth) in conjunction with the geographic location of the target object or target area, and the results are used as inputs for calculating the scattering angles, which are further used to assess the effectiveness of cloud parameter retrieval.

Based on the above analysis, we have established a relatively comprehensive analytical model for effective scattering angle prediction, which can predict the scattering angle coverage that can be observed at a certain location based on satellite observation information (satellite zenith angle and satellite azimuth angle) and solar information. The coverage of the effective scattering angle range for cloud parameter retrieval at the location is comprehensively assessed from five aspects: C-Det, cloud phase identification, C-RayPressure retrieval, and C-DSD retrieval. By predicting the coverage of the scattering angle and evaluating the validity of the scattering angle in the study area, it is possible not only to check whether the area is suitable for cloud characteristics retrieval but also to remove the parts that are not useful for the retrieval of a specific cloud parameter in advance, avoiding data redundancy.

Meanwhile, the load designer can also better realize the targeted design of the load according to the purpose of the load, for example, when the designer prefers to carry out the retrieval of the cloud microphysical structure through the observation of the load, the load with better effectiveness of the retrieval of the C-DSD can be selected according to our evaluation model to realize the retrieval of the cloud microphysical structure with higher accuracy.

In Fig. 14, the solar zenith angle is 40°, 60°, and 80°, and the scattering angle changes are observed when the zenith angle is between ±60° and the relative azimuth angle is between 0° and 90°. As we can see, given an observation zenith angle range,

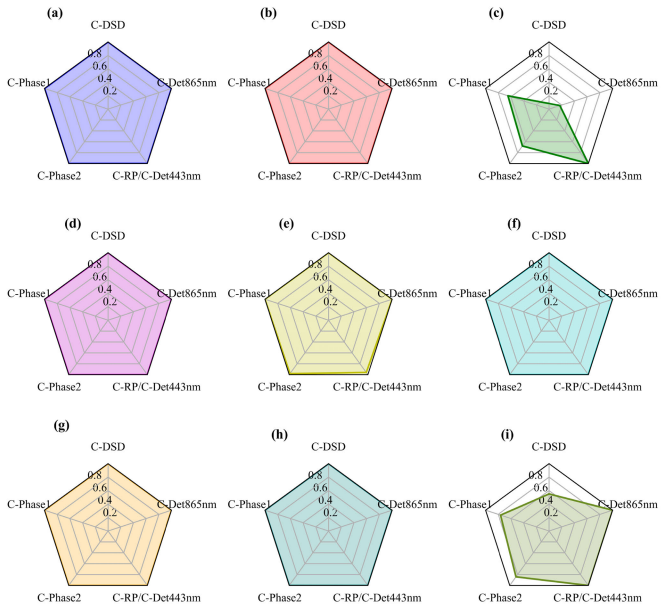

Fig. 15. Analysis results of scattering angle effectiveness in selected regions of the POLDER3/PARASOL, DPC/GF-5, and DPC/GF-5(02) orbits. (a)–(c) Results for POLDER-3 all-day data on July 26, 2013. (d)–(f) Results for DPC all-day data on March 4, 2020. (g)–(i) Results for DPC(02) all-day data on May 30, 2022.

a solar azimuth (solar zenith angle), and a relative azimuth range, a range of scattering angles for a given position or region can be obtained. According to the simulation results, the smaller the Sun zenith angle, the higher the maximum scattering angle.

With this model, we evaluate the effective scattering angle coverage of the cloud parameter retrieval over the scattering angle range of three regions (north, equator, and south) for the three loads, north represents the area between 50°N and 60°N, south represents the area between 35°S and 45°S, and equator represents the area between 10°N and 10°S. The evaluation results are shown in Fig. 15.

It can be found that among the three regions of the POLDER orbit, the scattering angle coverage of the north and equator regions shows high validity in the retrieval of the five cloud parameters, while the scattering angle coverage of the south region is less valid than that of the other two regions, and it only shows good validity in the retrieval of the cloud Rayleigh pressure and C-Det at 443 nm. This is mainly due to the fact that the POLDER observations only go up to about 50°S, and the south region is already in the more marginal region of the orbit, as also shown in Fig. 7.

The cloud parameter retrieval validity of DPC in the three selected regions is almost 100%. In two regions, north and equator, DPC(02) also demonstrates very high validity. However, in the south region, the validity of DPC(02) does not achieve full scores in all five aspects. This can be attributed to the distribution of the region with a high scattering angle of DPC(02) for the selected time, which is predominantly in the middle of the orbit to the north, while the high scattering angle region of DPC is distributed southward from the center of the orbit. Nevertheless, it is important to note that DPC(02) offers more observation angles than both POLDER and DPC, which is a notable advantage. In the future, the number of effective observation angles will be included as an additional evaluation factor.

V. Conclusion

The aim of the present research is to analyze the impact of orbital characteristics and viewing geometry on the retrieval of cloud properties from multiangle polarimetric measurements by measured data from three polarized multiangle loads [POLDER/PARASOL, DPC/GF-5, and DPC/GF-5(02)] and simulated data from radiative transfer mode. At the same time, we simulate and comprehensively evaluate the effectiveness of the polarized multiangle loaded orbital scattering coverage for the inversion of different cloud parameters by building an analytical model. The main conclusions are given as follows.

According to the simulation results of the ARTDECO radiative transfer model (liquid water cloud-Mie scattering theory and ice cloud-IHM model), the polarized radiative properties of clouds are highly sensitive to the scattering angle, and the polarization phase function and polarization reflectivity of water clouds change more drastically in the interval of effective scattering angle of cloud parameter inversion. Polarized multiangle loads can provide richer angular information, which greatly improves the accuracy of cloud parameters retrieval.

By analyzing the data of the three payloads POLDER-3/PARASOL, DPC/GF-5, and DPC/GF-5(02), we found the scattering angle distribution pattern of the three payloads orbits.

1) The scattering angle near the equator at low latitude is distributed between about 140° and 180°, which is much higher than that of the high-latitude region.
2) The scattering angle distribution shows a “radial,” the closer to the edge of the orbit, the lower the scattering angle.
3) For POLDER and DPC, the scattering angle on the west side of the orbit is higher than that on the east side of the orbit; for DPC(02), the scattering angle on the east side of the orbit is higher than that on the west side of the orbit.
4) The DPC and DPC(02) data have obvious angular advantages in the inversion of cloud droplet spectra.
5) Multiangle information is maximized when the scattering angle range is maximized.

According to the simulation and evaluation results of the analytical model, it can be seen that: the smaller the solar zenith angle is, the wider the coverage of the scattering angle is, which is more favorable to the inversion of cloud parameters; the polarization multiangle loads are very favorable to the inversion of cloud parameters, and for the north and equator regions, the validity of the three loads for the inversion of the five cloud parameters is all close to 100%. However, due to the orbital settings and observation angles, there is insufficient observation information for POLDER being at high latitudes in the south, and the validity of POLDER in this region is slightly lower than that of the DPC and DPC(02) angles in the evaluation results. If the number of observation angles is

used as an evaluation factor, the advantage of DPC(02) will be more prominent.

ACKNOWLEDGMENT

The authors would like to thank ICARE Data and Services Center, Villeneuve d'Ascq Cedex, France, for providing the POLDER-3/Parasol product (https://www.icare.univ-lille.fr/). Huazhe Shang conceived the idea of this study. Husi Letu and Huazhe Shang supervised the project. Yutong Wang performed the experiments and processed the data. Yutong Wang and Lesi Wei simulated the polarization properties of water and ice clouds. All contributed to the data analysis and the writing of this article.

REFERENCES

[1] M. B. Baker and T. Peter, "Small-scale cloud processes and climate," *Nature*, vol. 451, no. 7176, pp. 299–300, Jan. 2008, doi: 10.1038/nature06594.

[2] S. Mahajan and B. Fataniya, "Cloud detection methodologies: Variants and development—A review," *Complex Intell. Syst.*, vol. 6, no. 2, pp. 251–261, Dec. 2019, doi: 10.1007/s40747-019-00128-0.

[3] M. Quante, "The role of clouds in the climate system," *J. de Phys. IV (Proc.)*, vol. 121, pp. 61–86, Dec. 2004.

[4] W. B. Rossow and R. A. Schiffer, "Advances in understanding clouds from ISCCP," *Bull. Amer. Meteorolog. Soc.*, vol. 80, no. 11, pp. 2261–2288, Nov. 1999, doi: 10.1175/1520-0477(1999)080<2261:aiucfi>2.0.co.2.

[5] C. J. Stubenrauch et al., "Assessment of global cloud datasets from satellites: Project and database initiated by the GEWEX radiation panel," *Bull. Amer. Meteorolog. Soc.*, vol. 94, no. 7, pp. 1031–1049, Jul. 2013, doi: 10.1175/bams-d-12-00117.1.

[6] H. Wang and W. Su, "Evaluating and understanding top of the atmosphere cloud radiative effects in intergovernmental panel on climate change (IPCC) fifth assessment report (AR5) coupled model intercomparison project phase 5 (CMIP5) models using satellite observations," *J. Geophys. Res., Atmos.*, vol. 118, no. 2, pp. 683–699, Jan. 2013, doi: 10.1029/2012jd018619.

[7] G. Tana et al., "Retrieval of cloud microphysical properties from Himawari-8/AHI infrared channels and its application in surface shortwave downward radiation estimation in the sun glint region," *Remote Sens. Environ.*, vol. 290, May 2023, Art. no. 113548, doi: 10.1016/j.rse.2023.113548.

[8] C. Liu et al., "A cloud optical and microphysical property product for the advanced geosynchronous radiation imager onboard China's Fengyun-4 satellites: The first version," *Atmos. Ocean. Sci. Lett.*, vol. 16, no. 3, May 2023, Art. no. 100337, doi: 10.1016/j.aosl.2023.100337.

[9] C. Liu et al., "A machine learning-based cloud detection algorithm for the Himawari-8 spectral image," *Adv. Atmos. Sci.*, vol. 39, no. 12, pp. 1994–2007, Dec. 2022, doi: 10.1007/s00376-021-0366-x.

[10] C. Shi, T. Nakajima, and M. Hashimoto, "Simultaneous retrieval of aerosol optical thickness and chlorophyll concentration from multi-wavelength measurement over East China Sea," *J. Geophys. Res., Atmos.*, vol. 121, no. 23, pp. 14,084–14,101, Dec. 2016, doi: 10.1002/2016jd025790.

[11] T. Matsui, H. Masunaga, R. A. Pielke Sr, and W. K. Tao, "Impact of aerosols and atmospheric thermodynamics on cloud properties within the climate system," *Geophys. Res. Lett.*, vol. 31, no. 6, Mar. 2004, Art. no. L06109, doi: 10.1029/2003GL019287.

[12] H. Shen, H. Li, Y. Qian, L. Zhang, and Q. Yuan, "An effective thin cloud removal procedure for visible remote sensing images," *ISPRS J. Photogramm. Remote Sens.*, vol. 96, pp. 224–235, Oct. 2014, doi: 10.1016/j.isprsjprs.2014.06.011.

[13] O. Dubovik et al., "Polarimetric remote sensing of atmospheric aerosols: Instruments, methodologies, results, and perspectives," *J. Quant. Spectrosc. Radiat. Transf.*, vol. 224, pp. 474–511, Feb. 2019, doi: 10.1016/j.jqsrt.2018.11.024.

[14] X. Zhang, P. Zhang, Z. Fang, H. Qiu, X. Li, and Y. Zhang, "The progress in trace gas remote sensing study based on the satellite monitoring," *Meteorolog. Monthly*, Vol. 33, no. 7, pp. 3–14, Jul. 2007, doi: 10.3969/j.issn.1000-0526.2007.07.001.

[15] C. Shi, P. Wang, T. Nakajima, Y. Ota, S. Tan, and G. Shi, "Effects of ocean particles on the upwelling radiance and polarized radiance in the atmosphere-ocean system," *Adv. Atmos. Sci.*, vol. 32, no. 9, pp. 1186–1196, Sep. 2015, doi: 10.1007/s00376-015-4222-8.

[16] D. Clarke, J. Grainger, and S. S. Major, "Polarized light and optical measurement," *Am. J. Phys.*, vol. 40, no. 7, pp. 1055–1056, Jul. 1972, doi: 10.1016/C2013-0-02410-3.

[17] Z. Li et al., "Polarimetric satellite sensors for Earth observation and applications in atmospheric remote sensing," *J. Atmos. Environ. Opt.*, vol. 14, no. 1, pp. 2–17, Jan. 2019, doi: 10.3969/j.issn.1673-6141.2019.01.001.

[18] J. Gong, H. Zhan, and D. Liu, "A review on polarization information in the remote sensing detection," *Spectrosc. Spectral Anal.*, vol. 30, no. 4, pp. 1088–1095, Apr. 2010, doi: 10.3964/j.issn.1000-0593(2010)04-1088-08.

[19] B. Fougnie, "Improvement of the PARASOL radiometric in-flight calibration based on synergy between various methods using natural targets," *IEEE Trans. Geosci. Remote Sens.*, vol. 54, no. 4, pp. 2140–2152, Apr. 2016, doi: 10.1109/TGRS.2015.2496322.

[20] L. Chen et al., "Mission overview of the GF-5 satellite for atmospheric parameter monitoring," *Nat. Remote Sens. Bull.*, vol. 25, no. 9, pp. 1917–1931, Sep. 2021, doi: 10.11834/jrs.20210582.

[21] W. Yan, H. Yang, and X. Zhou, "A-train satellite formation and its application to cloud research," *Remote Sens. Inf.*, vol. 96, no. 2, pp. 93–96, Apr. 2008, doi: 10.3969/j.issn.1000-3177.2008.02.020.

[22] Z. Li et al., "Directional polarimetric camera (DPC): Monitoring aerosol spectral optical properties over land from satellite observation," *J. Quant. Spectrosc. Radiat. Transf.*, vol. 218, pp. 21–37, Oct. 2018, doi: 10.1016/j.jqsrt.2018.07.003.

[23] B. Fougnie et al., "The multi-viewing multi-channel multi-polarisation imager—Overview of the 3MI polarimetric mission for aerosol and cloud characterization," *J. Quant. Spectrosc. Radiat. Transf.*, vol. 219, pp. 23–32, Nov. 2018, doi: 10.1016/j.jqsrt.2018.07.008.

[24] T. Marbach, J. Riedi, A. Lacan, and P. Schlüssel, "The 3MI mission: Multi-viewing-channel-polarisation imager of the EUMETSAT polar system: Second generation (EPS-SG) dedicated to aerosol and cloud monitoring," *Proc. SPIE*, vol. 9613, pp. 271–278, Sep. 2015.

[25] D. J. Diner et al., "Advances in multiangle satellite remote sensing of speciated airborne particulate matter and association with adverse health effects: From MISR to MAIA," *J. Appl. Remote Sens.*, vol. 12, no. 4, Jul. 2018, Art. no. 042603, doi: 10.1117/1.jrs.12.042603.

[26] Y. Liu and D. J. Diner, "Multi-angle imager for aerosols: A satellite investigation to benefit public health," *Public Health Rep.*, vol. 132, no. 1, pp. 14–17, Jan. 2017, doi: 10.1177/0033354916679983.

[27] G. Milinevsky et al., "Calibration model of polarimeters on board the aerosol-UA space mission," *J. Quant. Spectrosc. Radiat. Transf.*, vol. 229, pp. 92–105, May 2019, doi: 10.1016/j.jqsrt.2019.03.007.

[28] G. Milinevsky et al., "New satellite project aerosol-UA: Remote sensing of aerosols in the terrestrial atmosphere," *Acta Astronautica*, vol. 123, pp. 292–300, Jun. 2016, doi: 10.1016/j.actaastro.2016.02.027.

[29] J. Werdell and A. deCharon, "PACE: How one NASA mission aligns with the united nations decade of ocean science for sustainable development (OceanShot #1)," *Mar. Technol. Soc. J.*, vol. 56, no. 3, pp. 118–121, Jun. 2022, doi: 10.4031/mtsj.56.3.30.

[30] S. Petro, K. Pham, and G. Hilton, "Plankton, aerosol, cloud, ocean ecosystem (PACE) mission integration and testing," in *Proc. IEEE Aerosp. Conf.*, Mar. 2020, pp. 1–20.

[31] D. G. Baldwin and J. A. Coakley, "Consistency of Earth radiation budget experiment bidirectional models and the observed anisotropy of reflected sunlight," *J. Geophys. Res., Atmos.*, vol. 96, no. D3, pp. 5195–5207, Mar. 1991, doi: 10.1029/90jd02414.

[32] N. G. Loeb and R. Davies, "Angular dependence of observed reflectances: A comparison with plane parallel theory," *J. Geophys. Res., Atmos.*, vol. 102, no. D6, pp. 6865–6881, Mar. 1997, doi: 10.1029/96jd03586.

[33] R. Stuhlmann, P. Minnis, and G. L. Smith, "Cloud bidirectional reflectance functions: A comparison of experimental and theoretical results," *Appl. Opt.*, vol. 24, no. 3, p. 396, Feb. 1985, doi: 10.1364/ao.24.000396.

[34] Á. Horváth and R. Davies, "Anisotropy of water cloud reflectance: A comparison of measurements and 1D theory," *Geophys. Res. Lett.*, vol. 31, no. 1, Jan. 2004, Art. no. L01102, doi: 10.1029/2003gl018386.

[35] P.-Y. Deschamps et al., "The POLDER mission: Instrument characteristics and scientific objectives," *IEEE Trans. Geosci. Remote Sens.*, vol. 32, no. 3, pp. 598–615, May 1994, doi: 10.1109/36.297978.

[36] M. Zhang et al., "Information content of ice cloud properties from multi-spectral, -angle and -polarization observations," *Remote Sens.*, vol. 12, no. 16, p. 2548, Aug. 2020, doi: 10.3390/rs12162548.

[37] M. Doutriaux-Boucher, J. Buriez, G. Brogniez, L. C. Labonnote, and A. J. Baran, "Sensitivity of retrieved POLDER directional cloud optical thickness to various ice particle models," *Geophys. Res. Lett.*, vol. 27, no. 1, pp. 109–112, Jan. 2000, doi: 10.1029/1999gl010870.

[38] F. Parol, J. Descloitres, and Y. Fouquart, "Cloud optical thickness and albedo retrievals from bidirectional reflectance measurements of POLDER instruments during ACE-2," *Tellus B*, vol. 52, no. 2, pp. 888–908, Apr. 2000, doi: 10.1034/j.1600-0889.2000.00026.x.

[39] J. D. Spinhirne, W. D. Hart, and D. L. Hlavka, "Cirrus infrared parameters and shortwave reflectance relations from observations," *J. Atmos. Sci.*, vol. 53, no. 10, pp. 1438–1458, May 1996, doi: 10.1175/1520-0469(1996)053<1438:cipasr>2.0.co.2.

[40] T. Cheng, L. Chen, X. Gu, T. Yu, and G. Tian, "Cloud phase classification and validation based on multi-angular polarized characteristics of cloud," *Acta Opt. Sin.*, vol. 28, no. 10, pp. 1849–1855, Oct. 2008, doi: 10.3321/j.issn:0253-2239.2008.10.003.

[41] F. Bréon and P. Goloub, "Cloud droplet effective radius from spaceborne polarization measurements," *Geophys. Res. Lett.*, vol. 25, no. 11, pp. 1879–1882, Jun. 1998, doi: 10.1029/98gl01221.

[42] H. Chepfer, G. Brogniez, and Y. Fouquart, "Cirrus clouds' microphysical properties deduced from POLDER observations," *J. Quantum Spectrosc. Radiat. Transf.*, vol. 60, no. 3, pp. 375–390, Sep. 1998, doi: 10.1016/S0022-4073(98)00013-2.

[43] P. Goloub et al., "Cloud thermodynamical phase classification from the POLDER spaceborne instrument," *J. Geophys. Res., Atmos.*, vol. 105, no. D11, pp. 14747–14759, Jun. 2000, doi: 10.1029/1999jd901183.

[44] L. Di Girolamo, L. Liang, and S. Platnick, "A global view of one-dimensional solar radiative transfer through oceanic water clouds," *Geophys. Res. Lett.*, vol. 37, no. 18, Sep. 2010, Art. no. L18809, doi: 10.1029/2010gl044094.

[45] S. Zeng, F. Parol, J. Riedi, C. Cornet, and F. Thieuleux, "Examination of POLDER/PARASOL and MODIS/Aqua cloud fractions and properties representativeness," *J. Climate*, vol. 24, no. 16, pp. 4435–4450, Aug. 2011, doi: 10.1175/2011jcli3857.1.

[46] M. D. Alexandrov, B. Cairns, C. Emde, A. S. Ackerman, and B. van Diedenhoven, "Accuracy assessments of cloud droplet size retrievals from polarized reflectance measurements by the research scanning polarimeter," *Remote Sens. Environ.*, vol. 125, pp. 92–111, Oct. 2012, doi: 10.1016/j.rse.2012.07.012.

[47] K. Knobelspiesse, B. Cairns, J. Redemann, R. W. Bergstrom, and A. Stohl, "Simultaneous retrieval of aerosol and cloud properties during the MILAGRO field campaign," *Atmos. Chem. Phys.*, vol. 11, no. 13, pp. 6245–6263, Jul. 2011, doi: 10.5194/acp-11-6245-2011.

[48] B. van Diedenhoven et al., "Remote sensing of ice crystal asymmetry parameter using multi-directional polarization measurements—Part 1: Methodology and evaluation with simulated measurements," *Atmos. Meas. Techn.*, vol. 5, no. 10, pp. 2361–2374, Oct. 2012, doi: 10.5194/amt-5-2361-2012.

[49] H. Shang et al., "Impact of cloud horizontal inhomogeneity and directional sampling on the retrieval of cloud droplet size by the POLDER instrument," *Atmos. Meas. Techn.*, vol. 8, no. 11, pp. 4931–4945, Nov. 2015, doi: 10.5194/amt-8-4931-2015.

[50] Y. Q. He, M. D. Jiang, X. Q. Hu, M. Q. Liu, W. Q. Jin, and Q. Hu, "Retrieval and analysis of MERSI polarization radiation characteristics based on ocean scene," *Acta Optica Sinica*, vol. 42, no. 6, pp. 238–248, Mar. 2022, Art. no. 0628002, doi: 10.3788/A0S202242.0628002.

[51] H. Letu et al., "Surface solar radiation compositions observed from Himawari-8/9 and Fengyun-4 series," *Bull. Amer. Meteorolog. Soc.*, vol. 104, no. 10, pp. E1772–E1789, Oct. 2023, doi: 10.1175/bams-d-22-0154.1.

[52] C. Shi, M. Hashimoto, K. Shiomi, and T. Nakajima, "Development of an algorithm to retrieve aerosol optical properties over water using an artificial neural network radiative transfer scheme: First result from GOSAT-2/CAI-2," *IEEE Trans. Geosci. Remote Sens.*, vol. 59, no. 12, pp. 9861–9872, Dec. 2021, doi: 10.1109/TGRS.2020.3038892.

[53] Z. Yang, Q. Gao, and P. Wang, "Polarization of reflected light by Earth objects," *Acta Optica Sinica*, vol. 25, no. 2, pp. 241–245, Feb. 2005, doi: 10.3321/j.issn:0253-2239.2005.02.022.

[54] S. Hioki et al., "Degree of ice particle surface roughness inferred from polarimetric observations," *Atmos. Chem. Phys.*, vol. 16, no. 12, pp. 7545–7558, Jun. 2016, doi: 10.5194/acp-16-7545-2016.

[55] L. C. Labonnote, G. Brogniez, M. Doutriaux-Boucher, J. Buriez, J. Gayet, and H. Chepfer, "Modeling of light scattering in cirrus clouds with inhomogeneous hexagonal monocrystals. Comparison with in-situ and ADEOS-POLDER measurements," *Geophys. Res. Lett.*, vol. 27, no. 1, pp. 113–116, Jan. 2000, doi: 10.1029/1999gl010839.

[56] L. C. Labonnote, G. Brogniez, J. Buriez, M. Doutriaux-Boucher, J. Gayet, and A. Macke, "Polarized light scattering by inhomogeneous hexagonal monocrystals: Validation with ADEOS-POLDER measurements," *J. Geophys. Res., Atmos.*, vol. 106, no. D11, pp. 12139–12153, Jun. 2001, doi: 10.1029/2000jd900642.

Yutong Wang received the B.Eng. degree in surveying and mapping engineering from Hohai University, Nanjing, China, in 2022. She is currently pursuing the Ph.D. degree in cartography and geographic information system (GIS) with the State Key Laboratory of Remote Sensing Science, Aerospace Information Research Institute, Chinese Academy of Sciences, Beijing, China.

Her research interests include satellite cloud remote sensing and radiative transfer mode.

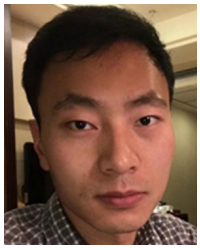

Huazhe Shang received the B.S. degree in remote sensing from Wuhan University, Wuhan, China, in 2011, and the Ph.D. degree in cartography and geographic information system from the University of Chinese Academy of Sciences, Beijing, China, in 2016.

His Ph.D. degree training included the retrieval of cloud droplet size distribution (C-DSD) using multiangle and polarization measurements from the POLarization and Directionality of Earth Reflectances (POLDER). In 2016, he joined the State Key Laboratory of Remote Sensing Science, Chinese Academy of Sciences, Beijing, where he was a Research Assistant. In 2019, he joined the Laboratoire d'Optique Atmosphérique, Univ. Lille, Lille, France, where he was a Visiting Scholar conducting research on cloud retrieval for the multiviewing, multichannel, and multipolarization imager (3MI). In 2020, he returned to China. His research interests include the detection of clouds and recognition of cloud phase information using measurements from geostationary satellites and the retrieval of liquid cloud properties from POLDER, 3MI, and directional polarimetric camera (DPC).

Husi Letu (Senior Member, IEEE) received the B.S. and M.S. degrees in geography from Inner Mongolia Normal University, Hohhot, China, in 1999 and 2002, respectively, and the Ph.D. degree in geosciences and remote sensing from the Center for Environmental Remote Sensing (CEReS), Chiba University, Chiba, Japan, in 2010.

He was with the Research and Information Center, Tokai University, Tokyo, Japan. He has been focusing on the algorithm development and validation of the ice cloud product for JAXA's GCOM-C and Himawari-8 satellite missions. He is currently a Professor with the State Key Laboratory of Remote Sensing Science, Aerospace Information Research Institute (AIR), Chinese Academy of Sciences (CAS), Beijing, China. His research interests include atmospheric radiative transfer, remote sensing, simulation of the optical properties of nonspherical particles, and retrieval of ice cloud property.

Lesi Wei received the B.S. and M.S. degrees from the Physics and Electronic Information College, Inner Mongolia Normal University, Hohhot, China, in 2013 and 2017, respectively.

He was a Research Assistant of sciences with the State Key Laboratory of the Science and Remote Sensing, Aerospace Information Research Institute, Chinese Academy of Sciences, Beijing, China. His research interests include satellite cloud remote sensing and radiative transfer mode.

Feinan Chen was born in Lu'an, Anhui, China, in 1986. He received the Ph.D. degree in optical engineering from the School of Electronic and Optical Engineering, Nanjing University of Science and Technology, Nanjing, Jiangsu, China, in 2015.

Since 2017, he has been an Assistant Researcher with the Anhui Institute of Optics and Fine Mechanics, Hefei Institutes of Physical Science, Chinese Academy of Sciences, Hefei, China, where he specializes in laboratory and inflight calibration of optical remote sensors.

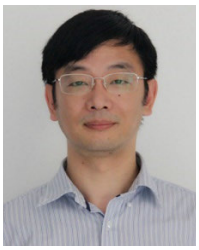

Jin Hong received the B.S. degree in communication engineering from Zhejiang University, Hangzhou, China, in 1987.

From 2006 to 2018, he completed the project of the directional polarimetric camera (DPC) as the Chief Engineer. Since 2004, he has been a Research Professor with the Anhui Institute of Optics and Fine Mechanics, Chinese Academy of Sciences, Hefei, China. Since 2018, he has been focusing on the research of polarization crossfire method for developing the particular matter polarization suits based on DPC and Scanning Polarimeter (ScanPol). His research interests include atmospheric aerosol polarimetric remote sensing.

Prof. Hong was a recipient of the 2020 Space Achievement Award by the China Space Foundation.

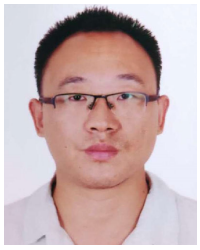

Zhongting Wang received the Ph.D. degree in cartography and geographical information system from the Institute of Remote Sensing Applications, Chinese Academy of Sciences, Beijing, China, in 2008.

He is currently a Senior Engineer of environmental remote sensing with the Satellite Environment Center, Ministry of Environmental Protection, Beijing. His research interests include atmospheric model simulations and atmospheric remote sensing.

Liangfu Chen received the Ph.D. degree in geography from the Institute of Remote Sensing and Geographic Information System (GIS), Peking University, Beijing, China, in 1999.

Since 2004, he has been leading the 863 Project of China, MultiSource Satellite Remote Sensing Technology of Atmospheric Pollution Monitoring, and the Knowledge Innovation Program, CAS, Beijing, where he is currently a Professor with the State Key Laboratory of Remote Sensing Science, Aerospace Information Research Institute. His research interests include the retrieval and application of atmosphere aerosol and trace gases based on remote sensing data.